Synchro-Excited Free-Running Single Photon Counting: A Novel Method for Measuring Short-Wave Infrared Emission Kinetics

Ching-Wei Lin,[†,§] Sergei M. Bachilo,[†] R. Bruce Weisman[†,‡,*]

[†] Department of Chemistry and the Smalley-Curl Institute, Rice University, Houston, TX 77005, United States

[‡] Department of Materials Science and NanoEngineering, Rice University, Houston, TX 77005, United States

[§] Present address: The David H. Koch Institute for Integrative Cancer Research, Massachusetts Institute of Technology, Cambridge, MA 02139, United States

ABSTRACT: Time-resolved measurements of short-wave infrared (SWIR) photoluminescence on the sub-microsecond to millisecond scale are needed for physical and chemical studies involving singlet oxygen, single-walled carbon nanotubes, and other samples with weak, slow emission. We present here an alternative to the common method of time-correlated single photon counting (TCSPC) that is well suited to indium gallium arsenide avalanche photodiode (APD) detectors operated in Geiger mode. In the new method, termed synchro-excited single photon counting (SEFR-SPC), excitation pulses from inexpensive laser diodes (providing a variety of wavelengths) are synchronized to detection events from a free-running detector covering the 900 to 1700 nm range. In contrast to TCSPC, data from this method can be rigorously corrected for pile-up distortions, allowing operation with high excitation powers and low repetition rates. A technique is described to extend the system's dynamic range to approximately 10^8. We also show that SEFR-SPC provides state-of-the-art sensitivity in the SWIR spectral region, and that spectrally filtered kinetic data can offer additional insights. A six-step correction protocol has been developed and implemented as a LabVIEW program for very accurate acquisition of kinetic shapes. The SEFR-SPC method will be a valuable tool for studies of weak, long-lived emission sources.

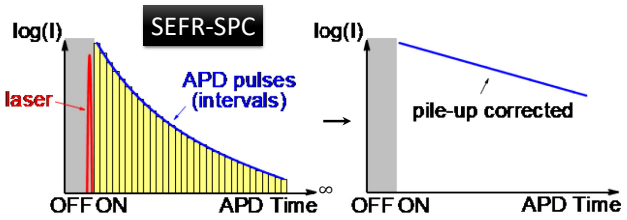

The spectral region from ca. 1000 to 1600 nm (often termed short-wave infrared or SWIR) is attractive for optical applications such as bio-imaging,[1,2] telecommunications,[3] and nondestructive inspection[4-6] because of favorable interactions with materials. For example, SWIR expands the detection window for optical imaging in biomedical research, offering improved image contrast through lower scattering and greatly reduced tissue autofluorescence.[7]

Many nanomaterials having SWIR luminescence can potentially be used as optical probes *in vivo*.[8-10] For example, single-wall carbon nanotubes (SWCNTs) show a variety of structure-dependent sharp SWIR emission peaks.[11-13] Beyond imaging applications, the method of time domain photon counting can enable fundamental studies in physical and analytical chemistry, such as the photophysics of SWIR-emissive SWCNTs and their triplet states. The detection of singlet oxygen emission at 1270 nm is also important and relevant for applications such as photodynamic therapy. However, optical studies of states with low radiative rates require sophisticated instrumentation that can distinguish weak delayed luminescence components from strong prompt fluorescence.

The typical method used in time-resolved SWIR photoluminescence experiments is to periodically excite the sample with short laser pulses and measure resulting luminescence profiles with specialized photomultipliers or avalanche photodiodes (APDs) based on Ge, SiGe, or InGaAs/InP.[14,15] The APDs may be either gated or free-running. Other special detectors include quantum dot devices, superconducting nanowires, and superconducting transition edge sensors.[15] It has been shown that gated mode InGaAs APDs potentially provide far higher signal-to-noise ratio than superconducting nanowire single photon detectors, presumably because they can suppress prompt signals.[16,17] Excitation and detection can be asynchronous in free-running mode or synchronous in gated mode. In the popular method of time-correlated single photon counting (TCSPC),[18] the delay between excitation pulse and the first detected luminescence photon is recorded for many events and compiled into a histogram revealing the sample's emission kinetics. Strong prompt interference from scattered excitation light can be blocked by an optical filter if its wavelength is not close to the emission of interest. Otherwise, a gated mode detector can be used to mask strong fluorescence in the active time window.[19] But this mode requires gate delay scans with narrow time windows, which significantly slows acquisition of complete kinetic curves. Also, relatively long dead times may be needed to prevent after-pulsing artifacts, leading to further acquisition inefficiency.

Here, we introduce a novel scheme for kinetic acquisition, synchronizing pulsed excitations to outputs from a free-running InGaAs APD detector. We call the method "synchro-excited free-running single photon counting," or SEFR-SPC. Depending on experimental needs, excitation laser pulses can be sent either within or after the detector dead period, and acquisition cycles are reinitialized when the detector senses a photon. This avoids the problems of low dynamic range in asynchronous excitation mode and reduced detection efficiency due to blinded pulses. Below we describe the optical and electronic designs and the data corrections needed to obtain reliable kinetic curves. Examples show how these corrections affect the quality of kinetic results. Notably, we use statistical survival analysis to achieve the first rigorous correction of errors caused by the pile-

up effect.[20-31] A detailed discussion compares SEFR to free-running and gated mode acquisitions.

DESIGN CONCEPT

Measurement scheme. For TCSPC measurements using a Geiger mode detector, the time histogram of photon counts may be distorted because only the first detected photon is registered per excitation cycle. This kinetic distortion, termed the pile-up effect, may be described using statistical survival analysis. If t is the time after excitation, the probability density $f(t)$ for detecting a photon in the interval $[t, t+dt]$ equals the product of the sample's true kinetic function $K(t)$ and the survival probability function $S(t)$. These are assumed independent of each other, so $f(t) = K(t)S(t)$. If the detector has survived to time t, it must detect a photon at or after time t. Therefore, the survival probability $S(t)$ is the sum of all probabilities for detecting a photon at or after time t, which can be written as

$$S(t) = \int_t^{\infty} f(\tau)\, d\tau \qquad (1)$$

Detection of a photon at time t prevents the detector from registering other photons for the rest of the cycle. Therefore, the survival probability for the detector remaining active decreases over time. Let $N(t)$ represent the measured number of detected photons in interval $[t, t+dt]$ summed over the many cycles of an experiment. As shown in Supporting Information page S-7, the relation between $K(t)$ and the measured counts $N(t)$ is

$$K(t) = \frac{N(t)}{\int_t^{\infty} N(u)\, du}. \qquad (2)$$

The relation shows that the pile-up effect can be corrected only if events at all times after t are recorded (from time t to ∞). This requirement can be met using our free-running mode acquisition, which always sets the detector active after its dead period until a photon has been detected. All acquisition cycles then have infinite effective integration times, and eq 2 can be used to recover the true kinetic function $K(t)$ from pile-up distorted raw data.

To illustrate this approach, Figure 1a shows the measured kinetic curve $N(t)$ of a constant light source using a deeply cooled free-running mode InGaAs APD detector. It is set to its inactive state for 27 µs of dead time after each avalanche event to allow recovery. The apparent near exponential decay reflects the decreasing survival function for the Geiger mode detector. Figure 1b shows the kinetic histogram deduced from the same data after pile-up correction using eq 2. This result properly indicates a near-constant count rate at times beyond 27 µs, with a value correctly matching the averaged count rate.

To apply eq 2 to kinetic (instead of constant) emission sources, the pulsed excitation must be synchronized to the APD output events. This ensures identical excitation in each acquisition cycle, allowing summation of all cycle data to construct the full $N(t)$ curve. The real kinetic curve $K(t)$ is then recovered using eq 2. This synchronized excitation with free-running detection is the core concept of the SEFR-SPC method.

Figure 2 shows the timing diagram for SEFR-SPC acquisition. The values τ_i are the intervals between adjacent APD pulses and are the only data recorded in the measurement. All other system timing parameters are pre-set and referenced to the APD pulses. Excitation laser pulses are sent at delay t_D with pulse width t_L. In Type 1 excitation (Figure 2a), laser pulses

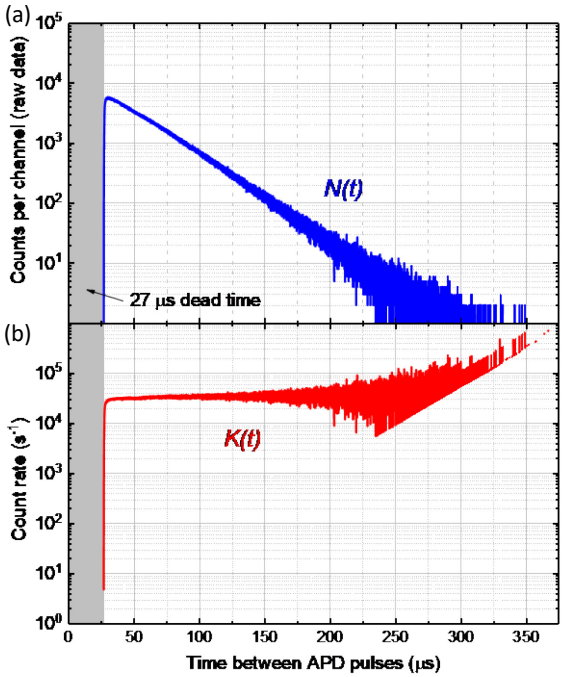

Figure 1. Analytical correction of pile-up distortion using eq 2 (Correction 1 in text). (a) Raw data for a constant intensity light source as measured with 20.08 ns channel resolution. Geiger-mode detection and pile-up distortion leads to apparent near-exponential decay in this case. The initial 27 µs shows no signal because it is the detector dead period. (b) Data after pile-up correction, showing recovery of near-constant count rate. Noise increases at longer times because of the lower survival probability of the APD at longer delays.

occur within the dead period. This is designed for measuring weak delayed luminescence accompanying strong prompt luminescence. By inducing the strong prompt emission during the dead period, we allow delayed luminescence to dominate the detection events. In Type 2 excitation (Figure 2b), laser pulses occur in the active window so that prompt luminescence is recorded. We also introduce forced trigger pulses after a specified active time window t_W to prevent extra wait time in cycles for which no photons are detected from the sample. Note that all events terminate if an APD pulse is received. In other words, each APD pulse reinitializes the system and starts the next detection cycle.

We use the survival model to correct for pile-up distortion in SEFR-SPC, whereas Poisson statistics is used in traditional TCSPC.[23] Even though the correction functions from these two models appear very different, we find they agree closely with each other (see Supporting Information). We also note that synchronized excitation/emission, which is the case for SEFR-SPC and gated mode TCSPC, allows correction of arbitrary kinetic curves using eq 2, unlike asynchronous acquisitions such as traditional free-running APD with independent excitations. (see discussion in Supporting Information p. S-10).

Instrument design. Figure 3a illustrates our system design for implementing SEFR-SPC. It contains four main components: an APD detector, a control circuit, two laser diodes, and a computer. The APD pulses have dual functions: signaling photon detection events, and triggering all other actions. The control circuitry is made of a commercial 48 MHz counter (20.8 ns res-

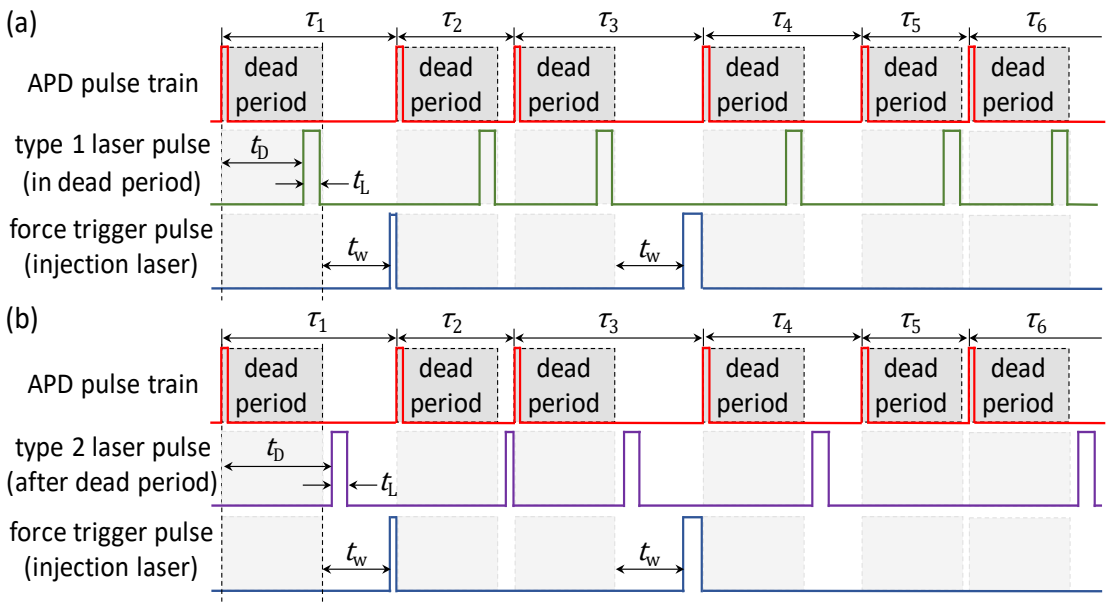

Figure 2. Timing diagrams for APD signals, laser excitations, and forced triggering. (a) In Type 1 measurements, which are used for samples giving intense prompt emission components, the excitation pulse is timed to occur within the detector's dead period by selection of trigger delay t_D and excitation pulse duration t_L. The number of APD pulses equals the number of excitations. (b) In Type 2 measurements, trigger delay t_D is set long enough that excitation laser pulses arrive after the detector dead period. If the next APD pulse occurs earlier, the control circuitry immediately turns off the excitation pulse. The force trigger pulses go to the injection laser to induce a detector event that defines the active time window t_W and resets the acquisition cycle. The values $\tau_1, \tau_2, \tau_3 \cdots$ are the intervals between adjacent APD pulses. Five different Type 2 conditions are illustrated: full excitation, short trigger (τ_1); partial excitation, no trigger (τ_2); full excitation, long trigger (τ_3); full excitation, no trigger (τ_4); and no excitation, no trigger (τ_5).

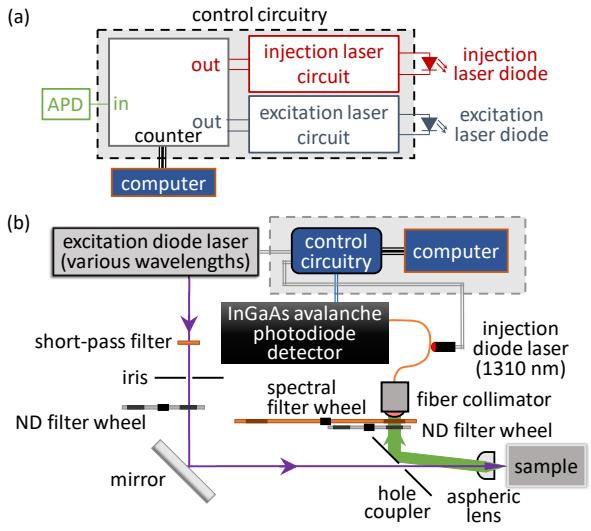

Figure 3. Instrument design. (a) The computer-interfaced control circuitry is composed of counter and laser driver circuits. The counter records the time intervals between successive APD pulses (labeled τ_i in Figure 2) and also generates signals to trigger the excitation laser and the injection laser that is used to force detector triggering. (b) Optical schematic diagram of the instrument.

olution) and simple drivers for generating laser pulses. The injection and excitation laser diodes are triggered by the APD pulses after desired delay times. The computer reads the sequence of time intervals τ_i from the counter and sets delay times t_D, t_L, and t_W in the counter.

Figure 3b shows the optical schematic diagram. The excitation beam is passed through a short-pass filter to remove stray SWIR light and its intensity is adjusted by a neutral density (ND) filter wheel. Then it passes through the hole of the beam coupler before being tightly focused into the sample by a fused silica aspheric lens. Use of the hole coupler and fused silica optics minimizes background emission from optical components and coatings. Sample luminescence is collected by the same aspheric lens, reflected at the hole coupler, and then focused into a fiber optic cable by the fiber collimator. To control the detected emission intensity and wavelengths, we place a 6 mm thick double filter wheel between the hole coupler and the fiber collimator. The collected emission is transmitted to a deep-cooled free-running Geiger mode InGaAs avalanche photodiode detector. The control circuitry sends and receives all electronic signals and communicates directly with the computer. Light from the 1310 nm diode laser is injected through the fiber optic wall to force detector triggering. Further details on the instrument are described in Supporting Information.

Correction protocols. We have developed 6 correction steps to optimize the accuracy and value of SEFR-SPC data (see Figure S4). These correct for: *1) pile-up distortion; 2) intrinsic background*; 3) *temporal sensitivity*; 4) *spectral response variation*; *5) limited dynamic range;* and *6) instrument response function*. Corrections 1-5 are stable for a given detector, whereas correction 6 also depends on instrument settings and needs to be recalibrated when they change. A further optional correction can be applied to remove signals from previous excitation pulses. In brief, intrinsic backgrounds including dark and after-pulsing are found to be significant when signals are low and time dependent. They are fixed for a given detector and can be corrected using measured data, as shown in Figures S6 and S7. Correction for

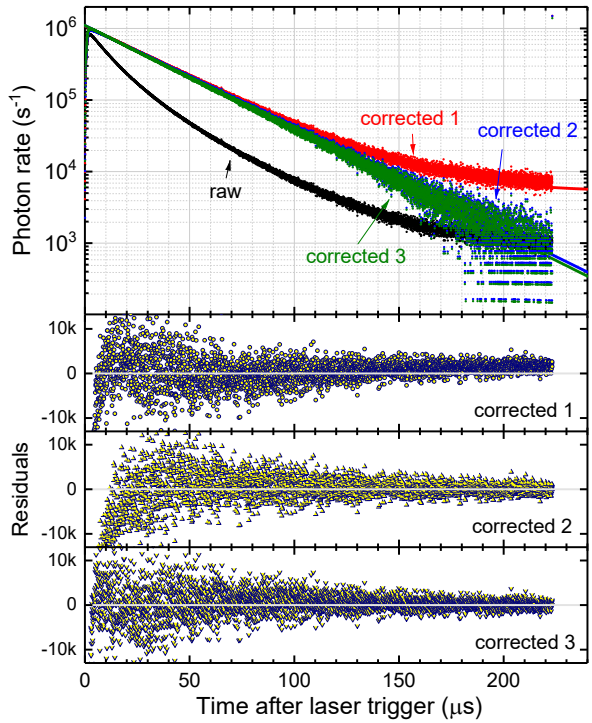

Figure 4. Data for singlet oxygen decay, shown at different stages of correction. The sample contained ~10 µM of C_{70} as a sensitizer in air-saturated toluene. Excitation pulses at 462 nm had full-widths at half-maximum of 110 ns (carrying ~22.7 nJ or $\mathbf{5.28 \times 10^{10}}$ photons) and arrived 1.42 µs after the end of the APD dead period. Corrected data sets are plotted with exponential best fits. Black symbols show raw data, uncorrected for pile-up distortions. The red "corrected 1" curve (apparent decay time of 30.90 µs) includes pile-up corrections. The "corrected 2" curve (30.02 µs) adds background correction. The green "corrected 3" curve (29.75 µs) also accounts for time-varying detector sensitivity. The three bottom frames show corresponding residuals between data and exponential fits. It was not necessary to apply an IRF correction here because excitation followed the dead period and the sample did not emit intense prompt luminescence that could distort measurements in this time range.

time dependent detector sensitivity is illustrated in Figures S8 and S9. We also correct for the wavelength dependent quantum efficiency of the detector (see Figure S10). A neutral density filter is used to attenuate the strong prompt emission to measure both prompt and delayed signals without detector saturation. We also can correct for the IRF because the whole decay curve is measured. Supporting Information contains detailed descriptions of the corrections, which are illustrated in the examples below.

RESULTS AND DISCUSSION

Importance of corrections. Figure 4 shows application of the corrections to measurement of the 1270 nm luminescence from $^1O_2$. In toluene, $^1O_2$ photosensitized by C_{70} has mono-exponential decay with a decay constant of ~29 µs.[32] The raw kinetic data decay much faster than this because of pile-up distortion, which is particularly severe in SWIR APDs, and the after-pulsing, which can also last many microseconds. The trace labeled "corrected 1" has been rigorously corrected to remove this distortion using eq 2. These data are rather well fit by an exponential decay plus offset, but the residuals plot shows systematic errors at long times, due mainly to a non-constant background. Trace "corrected 2" additionally has the intrinsic background subtracted (see Figure S7). The residuals are improved even though the apparent decay constant does not change significantly. Trace "corrected 3" includes the temporal sensitivity correction illustrated in Figures S8 and S9. This reduces the deduced time constant by 1 µs and makes the residuals symmetric about zero at all delays. The three combined corrections give the most reliable kinetic trace. Note that Correction 2 and 3 subtract or multiply correction factors directly to the kinetic curves without extra adjustment. Correction 4 can be applied to compare emission intensity data in different wavelength bands. Correction 5 (Figure S11) is appropriate for high dynamic range measurements, needed with samples that also show strong prompt emission (see next section).

Correction 6 (Figure S12) adjusts for the extra background from charge persistence[33,34] generated by photons arriving in the dead period. We have found that this IRF curve shape is constant over more than two orders of magnitude in excitation intensity (Figure S12b). IRF correction is important only when studying fast decay components with low intensities. We note that using a hole beam coupler in our optical design avoids background luminescence from a dichroic coating and greatly reduces the optical IRF contribution.

We estimate that the C_{70}-sensitized $^1O_2$ luminescence shown in Figure 4 represents ~32 detectable photons (corresponding to 32/0.135=237 arrived photons) for each excitation pulse of ~5.3×10^5 photons. The small detectable yield reflects the low photosensitizer concentration (giving a factor of ~10^{-2}), the mismatch of excitation and collection volumes due to lens chromatic aberration (unknown factor), the low quantum yield of $^1O_2$ luminescence (~1.6 x 10^{-4}),[35] loss from the hole coupler (~0.33), losses at the surfaces of lenses and band-pass filters (~0.8) and the finite collection aperture (~10^{-2}). More than >90% of the excitation light was not absorbed or was absorbed outside of the collection volume. The remaining main loss comes from the small detector étendue. We estimate that our overall detection factor is around 3700 Hz mW^{-1} of excitation power. Comparing with recent reported values for a free-running APD (350 Hz mW^{-1} for rose bengal in H_2O)[17] and superconducting nanowire detectors (3 Hz mW^{-1} for rose bengal in H_2O)[16], our instrument shows an optical efficiency at least 1.1 to 129 times higher than those state-of-the-art instruments.

Spectrally-filtered kinetic curves, high dynamic range, and wide active window. Our instrument can capture kinetics in different wavelength ranges using several band pass filters, a method we call spectrally-filtered SEFR-SPC. To illustrate, Figure 5 shows the luminescence spectrum and kinetics of methylene blue (MB) in O_2-saturated D_2O. MB is an FDA-approved drug for treating methemoglobinemia and is also commonly used as a photosensitizer for generating $^1O_2$ in water. Figure 5a plots the absorption and luminescence spectra of MB in D_2O saturated either with argon or oxygen. The O_2-saturated sample shows a $^1O_2$ luminescence peak at 1275 nm, which is absent for the Ar-saturated sample. The broad spectrum in the Ar-saturated sample represents the prompt fluorescence emission of MB in the SWIR. An intriguing increased intensity of the broad MB emission is observed on O_2 purging. We suggest that this higher intensity is delayed fluorescence of MB as $^1O_2$

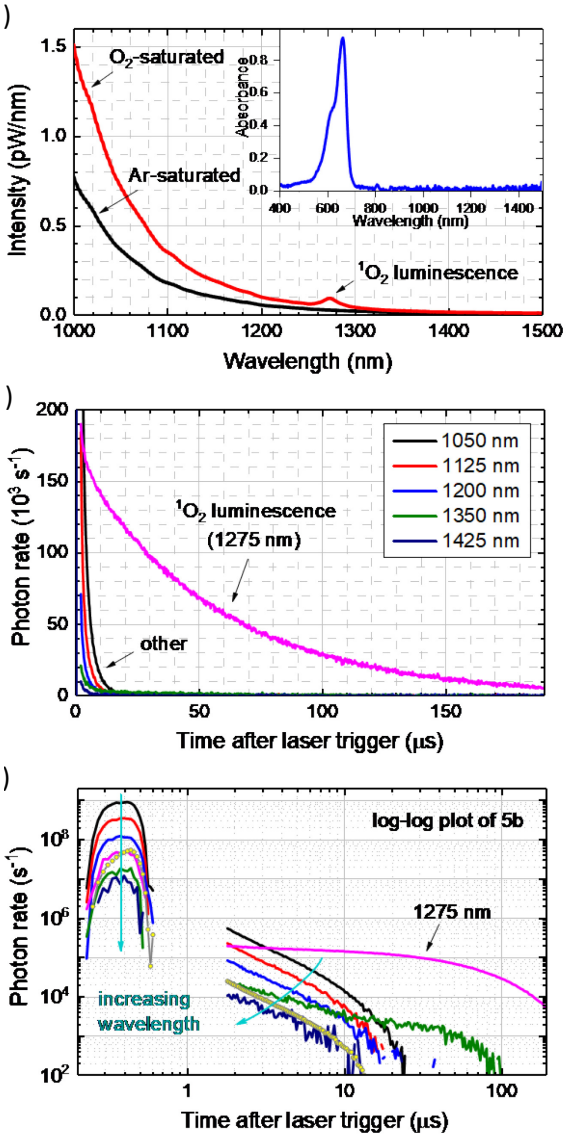

Figure 5. Photoluminescence of methylene blue (MB) in O_2-saturated D_2O. (a) SWIR spectrum measured with continuous 660 nm excitation. A control spectrum taken after purging with argon is shown for comparison. (inset) Absorption spectrum of the MB solution in 1 cm path fused silica cuvette. (b) SWIR emission kinetics measured through several spectral filters. Singlet oxygen luminescence at 1275 nm shows mono-exponential decay with a decay constant of 56.5 µs. (c) Log-log plots of the data from frame (b). Blue arrows cross data curves in the order of 1050, 1125, 1200, 1350, and 1425 nm, which show mainly the IRF. The tail at 1350 nm (green) contains residual $^1O_2$ luminescence plus IRF. The measured IRF (gray open circles) was normalized to the prompt luminescence at 1275 nm, showing that the 1275 nm luminescence is a factor of 10 above the IRF background at 2 µs. Here, the $^1O_2$ decay constant should be found either after subtracting the IRF component or by analyzing only data after ~10 µs. The high dynamic range measurements were made by hiding strong MB prompt luminescence in the detector dead period.

back-sensitizes the photosensitizer triplet state under continuous excitation. This phenomenon has been reported by Scholz *et al*.[36] To check, we subtracted the spectra of O_2-saturated from Ar-saturated samples and compared with the original Ar-saturated spectrum. The shapes of these two spectra are well matched after normalization except for the singlet oxygen peak (Figure S16a), supporting the delayed fluorescence hypothesis. Figure 5b shows the spectrally-filtered SEFR-SPC kinetic curves in the SWIR (with level 4 corrections). The curve at 1275 nm reveals strong $^1O_2$ luminescence.

Several other spectral regions centered at 1050, 1125, 1200, 1350, and 1425 nm were also monitored and showed fast decaying curves with a time constant of ~1.5 µs over the first 20 µs. The intensities of these fast decay curves were greater at shorter wavelengths, following the same trend observed for delayed fluorescence in continuous spectral measurements. This emission may represent either delayed fluorescence from MB or part of our system's IRF made evident by strong prompt emission. To distinguish these possibilities, we measured kinetic traces of the prompt luminescence and constructed the whole prompt + delayed luminescence curve (correction 5 shown in Figure 5c). By comparing those curves to the normalized IRF, we identified the fast decaying tails as mainly from IRF (correction 6 as shown in Figure S16b). The intensities of these IRF tails depend linearly on the prompt signal intensities, so they should follow the same trend as the continuous emission spectrum. The triplet state MB concentration falls quickly to near zero if the oxygen concentration exceeds that of MB. We estimate an O_2 concentration in our samples of 1.27 mM, while the MB concentration is far lower at ~13 µM.[37] Hence, $^1O_2$ back-sensitization is not expected here. The IRF signal tails in the presence of MB make it necessary to carefully account for the IRF when extracting decay kinetics of $^1O_2$ in H_2O, which occurs on the same time scale.

Spectrally resolved SEFR-SPC data give extra information for photodynamics studies and can distinguish emission from different SWCNT structures. We use several band pass filters instead of a grating system to gain optical efficiency at the expense of spectral resolution. This sensitivity is needed to study processes such as triplet-triplet annihilation, where delayed fluorescence can be more than 1000 times weaker than prompt fluorescence and decays within several microseconds.[38] When studying such delayed emission, it is necessary to "blind" the detector against strong prompt fluorescence.

Photosensitizer flexibility. Various photosensitizers may be needed in photophysical research to satisfy experimental constraints such as solubility, toxicity, and reactivity. The apparatus described here supports many photosensitizers through flexible choice of excitation wavelength, which is limited only by commercial availability of laser diodes. We illustrate this versatility with time-resolved emission measurements on $^1O_2$ generated by different photosensitizers: C_{70} in toluene (462 nm excitation), methylene blue (MB) in D_2O (660 nm excitation), and rose bengal in D_2O and in ethanol (520 nm excitation). Figure 6 shows the set of normalized kinetic histograms for $^1O_2$ luminescence. $^1O_2$ in toluene is known to have a decay constant of ~29 µs. The triplet state of C_{70} sensitizer in air-saturated solution is efficiently quenched by dissolved ground state oxygen ($\phi \sim 1$), so we did not observe C_{70} phosphorescence. (see Figure S17). We chose to excite C_{70} at 462 nm because wavelengths below 400 nm may induce SWIR luminescence from trace impurities in quartz (glass) cells. Our $^1O_2$ luminescence data for MB in D_2O show a decay time of 55.5 µs, which is near the average of values reported in the literature.[32] Even though MB

emits strong prompt fluorescence, it is still easy to extract the much longer decay constant for weak emission.

In the case of rose bengal in ethanol, $^1O_2$ luminescence shows a 13.9 µs decay constant, which matches published values.[32] Changing the solvent to air-saturated H_2O requires more careful measurement because rose bengal has a triplet lifetime below ~2.4 µs, in the same range as that of $^1O_2$.[36] We therefore set the excitation pulses as short as possible, 20 ns, to suppress any rose bengal SWIR phosphorescence tail. $^1O_2$ is formed by energy transfer from the sensitizer and decays mainly by first-order nonradiative relaxation, so its concentration follows A ® B ® C kinetics. Our measured $^1O_2$ lifetime in H_2O of 3.2 µs agrees with recent reported values.[16,39]

Comparison of free-running, gated, and SEFR methods. Both traditional free-running and gated-mode kinetic acquisition use periodic excitation. This is not only simpler, but is also required in many cases, as when prevention of pile-up distortion requires low detection probabilities and high excitation rates. Unlike traditional periodic excitation, SEFR-SPC synchronizes the excitations to non-periodic detector events. The time reference is re-zeroed after each detector pulse, and the sequence of time intervals between detector pulses constitutes the complete data set, which can be readily converted into a kinetic histogram. This can then be analytically corrected for pile-up distortions to obtain a proper kinetic curve.

After-pulsing of InGaAs APD detectors gives a microsecond-scale tail after detection events, which can lead to another type of artifact in asynchronous free-running mode. Increasing the dead time setting is the most common way to avoid this problem. However, we find that after-pulsing in our detector continues for more than 25 µs (Figure S6a). Setting the dead time to such a long value in asynchronous mode would cause low measurement efficiency and excessive sample irradiation. Therefore, asynchronous free-running measurements involve a trade-off between efficiency and after-pulsing backgrounds.

Another drawback of asynchronous excitation mode is limited dynamic range, caused when strong prompt luminescence gives lower detection probability and extra background at later times. Traditional gated-mode acquisition can avoid these problems by synchronizing a narrow scanned detection window to the periodic excitation pulses, blocking any strong prompt luminescence.[19] However, this mode can be inefficient because only a small fraction of emission events are detected.

SEFR-SPC can be optimized for high dynamic range measurements by sending excitations just before the end of the detector dead period. This feature is similar to the gated mode, but the long active window in SEFR-SPC leads to high acquisition efficiency. Another factor aiding SEFR-SPC efficiency is that excitation occurs only when the APD is ready to detect. The detector dead time can therefore be increased without causing ineffective excitations, although increased dead times do lower the repetition rate and reduce average excitation power. One can compensate by raising the peak excitation power because pile-up distortion is fully correctable.

The main parameter hampering SEFR-SPC acquisition efficiency is the detector dark count rate. Higher dark rates limit the active detection window, so measuring kinetics on the millisecond scale requires reducing the dark counts by cooling the detector or lowering its efficiency setting. Also, the single window character of each cycle reduces the signal-to-noise ratio at

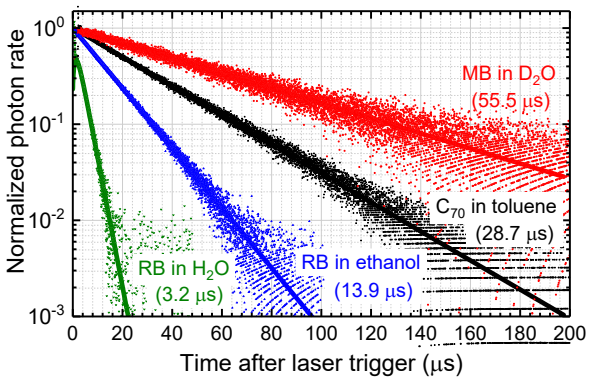

Figure 6. Singlet oxygen luminescence data, corrected as described in the text, measured in different solvents using methylene blue (MB), rose bengal (RB), and C_{70} as photosensitizers. C_{70}, RB, and MB were excited with 462, 520, and 660 nm lasers, respectively. $^1O_2$ in H_2O shows non-exponential kinetics due to slower oxygen diffusion and faster singlet oxygen decay.

longer times because of low survival probability. Another drawback of our instrument is its relatively coarse time resolution. This has no obvious disadvantage for measuring slow delayed luminescence, but it limits studies of prompt fluorescence. However, the time resolution could be greatly improved by using faster, sub-nanosecond counter electronics.

Unlike traditional free-running and gated mode instruments, our SEFR-SPC design uses relatively simple control circuitry. The cost for the whole instrument entails a free-running InGaAs APD (~$20,000), a counter (~$300), and optical components (~$1000). No high repetition rate laser or start-stop time-to-digital converter is required. Table 1 shows a more complete comparison of the three methods. Again, SEFR-SPC preserves the free-running properties while retaining some advantages of synchronized gated mode. Its design concept is opposite that of traditional TCSPC, as SEFR-SPC uses high excitation energy at low repetition rate to achieve high acquisition efficiency, whereas TCSPC uses low excitation energy at high repetition rate. SEFR-SPC is thus well suited to delayed luminescence studies and may be more economical to implement than other designs.

CONCLUSIONS

We have demonstrated a novel synchro-excited free-running single photon counting (SEFR-SPC) method that is optimized for kinetic measurements of delayed luminescence in the short-wave infrared (SWIR). SEFR-SPC synchronizes excitations to the APD detector pulses, which, in combination with optical filtering, gives a dynamic range of up to 10^8 on sub-microsecond to millisecond time scales. We also present a six-step data correction protocol to solve pile-up distortions, subtract time-dependent background, correct for time-dependent sensitivity, rescale for wavelength-dependent sensitivity (quantum efficiency), obtain high dynamic range, and eliminate the instrument response function tail caused by detector charge persistence. These corrections enable the determination of accurate kinetic parameters, some of which could not be found using traditional free-running and gated mode detection. Most notable is the rigorous correction for pile-up distortions, allowing high collection efficiency at low repetition rates.

Table 1. Comparison of Data Acquisition Methods for Time-resolved Photoluminescence Measurements

Function or Property	Synchro-excited free-running (SEFR)	Asynchronous free-running	Gated
Active trigger source	detection event	laser or pulse generator	laser or pulse generator
Detect photons after strong signal?	yes	no	yes
Dynamic range	high (~10^8)	low (~10^3)	high
Time resolution	sub-µs	sub-ps	sub-ps
Excitation cycle efficiency [c]	high	moderate	low
Laser-detector synchronization	synchronous	asynchronous	synchronous
Some wasted excitation pulses?	no	yes	yes
Pile-up distortions	rigorously correctable	inevitable except at low detection probability	inevitable unless time window defined as channel width
Excitation repetition	synchronized to detector	periodic	periodic
Excitation repetition rate	low (from background freq. to dead time freq.) [a]	high	high
Excitation pulse width	counter resolution [b] to ∞	ps to ∞	ps to ∞
Expense	relatively low	moderate	moderate
Applications	prompt and delayed luminescence	prompt luminescence	prompt and delayed luminescence

[a] The background count frequency is from ~500 to ~2000 Hz and the frequency of dead time is ~37 kHz with the dead time set to 27 µs.
[b] Resolution depends on counter electronics; it is 20.1 ns in this work.
[c] Defined as the number of detected photons per excitation pulse. This equals 1 for SEFR-SPC and ~0.05 for TCSPC.

Spectrally-resolved SEFR-SPC data on delayed SWIR luminescence enables more detailed photophysical studies of materials such as singlet oxygen, single-wall carbon nanotubes, and photosensitizers. The use of simple laser diodes as excitation sources provides multiple wavelengths, variable pulse widths, and suitable pulse energies at modest cost. Epiluminescence optics combined with a hole beam coupler capture signals from small sample volumes while maintaining high signal-to-noise ratios. This gives the potential for localized sample analysis such as single particle counting or fluorescence correlation spectroscopy (see Figure S19). With excitation synchronized to detector output pulses, the SEFR-SPC control circuitry is very simple. This keeps the total instrument cost low without compromising acquisition efficiency or signal-to-noise ratio. Improved time resolution can be achieved when needed by using faster counter electronics.

MATERIALS AND METHODS

Materials. C_{70} was purchased from MER Corp. (99+% purity). Methylene blue was from Fisher Scientific (90% purity; Lot 884666). Rose bengal was from Chem-Impex International, Inc. (91.0% purity; Lot 002126-03-33). Toluene was from Honeywell Burdick & Jackson (99.8% purity; Lot DC292). Ethanol was from Pharmo-Aaper (99.98% purity; Lot C1303042). Quartz cuvettes were cleaned with Chromerge to fully remove organic residuals before use. We used rose bengal solutions within one day of preparation for all measurements.

Instrument setup and components. A temperature-controlled mount (Thorlabs TLCDM9) was used to maintain laser diodes at 18°C. The multimode laser diodes included emission wavelengths of 462 nm (1.4 W), 520 nm (700 mW), 638 nm (700 mW), 660 nm (300-400 mW), and 808 nm (300 mW). The AR-coated, 10 mm e.f.l. fused silica aspheric lens was purchased from Edmund Optics (#87-991). The hole beam coupler was custom-fabricated by drilling a 2 mm hole at 45 degrees in the center of a silver-coated first-surface mirror. Several hard coated OD4 50 nm bandpass filters from Edmund Optics, including central wavelengths at 1050, 1125, 1200, 1275, 1350, and 1425 nm, were mounted on a filter wheel (Edmund #58-183) to select desired wavelength ranges. All three filter wheels for excitation attenuation, emission attenuation, and emission spectral selection were motorized using stepper gear-motors (StepperOnline, gear ratio 5:1) and a controller board (Printrbot Printrboard Rev. F6). An aspheric lens fiber collimator (Thorlabs CFC-11X-C) collected the emission and launched it into the 105 µm core of a step-index optical fiber (Thorlabs M43L01). We removed one 5 mm section of the fiber jacket to allow entry of light from an injection diode laser that forced detector triggering. An InGaAs free-running Geiger mode avalanche photodiode (ID Quantique ID220) was used to detect SWIR emission. All reflective mirrors were metallic and all optics exposed to excitation light were made of fused silica. The counter module (Measurement Computing MC-CTR08) was configured to count APD pulses and control the lasers. The entire optical system was baffled against ambient light. We used

a 45 W NIST-traceable calibrated quartz tungsten halogen lamp (Oriel Model 63358) to calibrate the wavelength-dependent detector quantum efficiency. Absorption spectra were measured on a prototype NS2 NanoSpectralyzer (Applied NanoFluorescence).

ASSOCIATED CONTENT

Supporting Information

The Supporting Information is available free of charge on the ACS Publications website.

Detailed description of the instrument design and SEFR-SPC controlling circuits; Derivation of equations for pile-up correction; Estimation of collection efficiency; Descriptions and calibration curves for all six steps of data correction protocol; Additional figures of singlet oxygen and SWCNT kinetics; Figure showing single particle counting of SWCNTs; Additional tables of laser and detector parameters (PDF)

AUTHOR INFORMATION

Corresponding Author

* E-mail: weisman@rice.edu.

ORCID

Ching-Wei Lin: 0000-0001-5646-1007
Sergei M. Bachilo: 0000-0001-5236-1383
R. Bruce Weisman: 0000-0001-8546-9980

Notes

The authors declare no competing financial interests.

ACKNOWLEDGMENTS

The authors thank Dr. Kathleen M. Beckingham for fruitful discussions and providing essential chemicals. This research was supported by grants from the National Science Foundation (CHE-1409698 and CHE-1803066) and the Welch Foundation (C-0807).

REFERENCES

(1) Gong, M.; Zhou, W.; Kenney, M. J.; Kapusta, R.; Cowley, S.; Wu, Y.; Lu, B.; Lin, M.-C.; Wang, D.-Y.; Yang, J.; Hwang, B.-J.; Dai, H. Blending Cr_2O_3 into a NiO-Ni Electrocatalyst for Sustained Water Splitting *Angew. Chem., Int. Ed.* **2015**, *54*, 11989-11993.

(2) Lin, C.-W.; Bachilo, S. M.; Zheng, Y.; Tsedev, U.; Huang, S.; Weisman, R. B.; Belcher, A. M. Creating Fluorescent Quantum Defects in Carbon Nanotubes using Hypochlorite and Light *Nat. Commun.* **2019**, *10*, 2874.

(3) Sugawara, M.; Hatori, N.; Ishida, M.; Ebe, H.; Arakawa, Y.; Akiyama, T.; Otsubo, K.; Yamamoto, T.; Nakata, Y. Recent Progress in Self-Assembled Quantum-dot Optical Devices for Optical Telecommunication: Temperature-insensitive 10 Gb s^{-1} Directly Modulated Lasers and 40 Gb s^{-1} Signal-regenerative Amplifiers *J. Phys. D: Appl. Phys.* **2005**, *38*, 2126-2134.

(4) Šašić, S.; Ozaki, Y. Short-Wave Near-Infrared Spectroscopy of Biological Fluids. 1. Quantitative Analysis of Fat, Protein, and Lactose in Raw Milk by Partial Least-Squares Regression and Band Assignment *Anal. Chem.* **2001**, *73*, 64-71.

(5) Sun, P.; Bachilo, S. M.; Lin, C.-W.; Weisman, R. B.; Nagarajaiah, S. Noncontact Strain Mapping using Laser-induced Fluorescence from Nanotube-based Smart Skin *J. Struct. Eng.* **2019**, *145*, 04018238.

(6) Sun, P.; Bachilo, S. M.; Lin, C.-W.; Nagarajaiah, S.; Weisman, R. B. Dual-layer Nanotube-based Smart Skin for Enhanced Noncontact Strain Sensing *Struct Control Health Monit.* **2019**, *26*, e2279.

(7) Vo-Dinh, T.; CRC Press: Boca Raton, FL, 2003.

(8) Villa, I.; Vedda, A.; Cantarelli, I. X.; Pedroni, M.; Piccinelli, F.; Bettinelli, M.; Speghini, A.; Quintanilla, M.; Vetrone, F.; Rocha, U.; Jacinto, C.; Carrasco, E.; Rodriguez, F. S.; Juarranz, A.; del Rosal, B.; Ortgies, D. H.; Gonzalez, P. H.; Sole, J. G.; Garcia, D. J. 1.3 μm Emitting SrF_2:Nd^{3+} Nanoparticles for High Contrast *In Vivo* Imaging in the Second Biological Window *Nano Res.* **2015**, *8*, 649-665.

(9) Hong, G. S.; Antaris, A. L.; Dai, H. J. Near-infrared Fluorophores for Biomedical Imaging *Nat. Biomed. Eng* **2017**, *1*, 0010.

(10) Dang, X.; Bardhan, N. M.; Qi, J.; Gu, L.; Eze, N. A.; Lin, C.-W.; Kataria, S.; Hammond, P. T.; Belcher, A. M. Deep-tissue Optical Imaging of Near Cellular-sized Features *Sci. Rep.* **2019**, *9*, 3873.

(11) Bachilo, S. M.; Strano, M. S.; Kittrell, C.; Hauge, R. H.; Smalley, R. E.; Weisman, R. B. Structure-assigned Optical Spectra of Single-walled Carbon Nanotubes *Science* **2002**, *298*, 2361-2366.

(12) Lin, C.-W.; Bachilo, S. M.; Vu, M.; Beckingham, K. M.; Weisman, R. B. Spectral Triangulation: a 3D Method for Locating Single-walled Carbon Nanotubes In Vivo *Nanoscale* **2016**, *8*, 10348-10357.

(13) Lin, C.-W.; Yang, H. L.; Sanchez, S. R.; Mao, W. Q.; Pang, L.; Beckingham, K. M.; Bast, R. C.; Weisman, B. In Vivo Optical Detection and Spectral Triangulation of Carbon Nanotubes *ACS Appl. Mater. Interfaces* **2017**, *9*, 41680-41690.

(14) Hiskett, P. A.; Buller, G. S.; Loudon, A. Y.; Smith, J. M.; Gontijo, I.; Walker, A. C.; Townsend, P. D.; Robertson, M. J. Performance and Design of InGaAs/InP Photodiodes for Single-photon Counting at 1.55 μm *Appl. Opt.* **2000**, *39*, 6818-6829.

(15) Kapusta, P.; Wahl, M.; Erdmann, R. *Advanced Photon Counting: Applications, Methods, Instrumentation*; Springer, 2015; Vol. 15.

(16) Gemmell, N. R.; McCarthy, A.; Liu, B. C.; Tanner, M. G.; Dorenbos, S. D.; Zwiller, V.; Patterson, M. S.; Buller, G. S.; Wilson, B. C.; Hadfield, R. H. Singlet oxygen luminescence detection with a fiber-coupled superconducting nanowire single-photon detector *Opt. Express* **2013**, *21*, 5005-5013.

(17) Boso, G.; Ke, D. M.; Korzh, B.; Bouilloux, J.; Lange, N.; Zbinden, H. Time-resolved Singlet-oxygen Luminescence Detection with an Efficient and Practical Semiconductor Single-photon Detector *Biomed. Opt. Express* **2016**, *7*, 211-224.

(18) Becker, W. *Advanced Time-correlated Single Photon Counting Techniques*; Springer Science & Business Media, 2005; Vol. 81.

(19) Lunghi, T.; Pomarico, E.; Barreiro, C.; Stucki, D.; Sanguinetti, B.; Zbinden, H. Advantages of Gated Silicon Single-photon Detectors *Appl. Opt.* **2012**, *51*, 8455-8459.

(20) Coates, P. B. The Correction for Photon 'Pile-up' in the Measurement of Radiative Lifetimes *J. Phys. E: Sci. Instrum.* **1968**, *1*, 878.

(21) Davis, C. C.; King, T. A. Single Photon Counting Pileup Corrections for Time-Varying Light Sources *Rev. Sci. Instrum.* **1970**, *41*, 407-408.

(22) Davis, C. C.; King, T. A. Correction Methods for Photon Pile-up in Lifetime Determination by Single-photon Counting *J. Phys. A: Gen. Phys.* **1970**, *3*, 101-109.

(23) Coates, P. B. Pile-up Corrections in the Measurement of Lifetimes *J. Phys. E: Sci. Instrum.* **1972**, *5*, 148-150.

(24) Coates, P. B. Pile-up Corrections in Lifetime Experiments *Rev. Sci. Instrum.* **1972**, *43*, 1855-1856.

(25) Davis, C. C.; King, T. A. Photon Pile-up Corrections in the Study of Time-varying Light Sources *J. Phys. E: Sci. Instrum.* **1972**, *5*, 1072-1074.

(26) Harris, C.; Selinger, B. Single-Photon Decay Spectroscopy. II. The Pile-up Problem *Aust. J. Chem.* **1979**, *32*, 2111-2129.

(27) Salthammer, T. Numerical Simulation of Pile-up Distorted Time-correlated Single Photon Counting (TCSPC) Data *J. Fluoresc.* **1992**, *2*, 23-27.

(28) Arlt, J.; Tyndall, D.; Rae, B. R.; Li, D. D.-U.; Richardson, J. A.; Henderson, R. K. A Study of Pile-up in Integrated Time-correlated Single Photon Counting Systems *Rev. Sci. Instrum.* **2013**, *84*, 103105.

(29) Donohue, D. E.; Stern, R. C. Correction of Single Photon or Particle Timing Measurements for Multiparticle Events *Rev. Sci. Instrum.* **1972**, *43*, 791-796.

(30) Meurs, B. v.; Werf, R. v. d. A Circuit for Rejecting Multiple Events Detected during a Timing Cycle in Single Photon Counting Experiments *J. Phys. E: Sci. Instrum.* **1976**, *9*, 437-438.

(31) Sergent, N.; Levitt, J. A.; Green, M.; Suhling, K. Rapid Wide-field Photon Counting Imaging with Microsecond Time Resolution *Opt. Express* **2010**, *18*, 25292-25298.

(32) Wilkinson, F.; Helman, W. P.; Ross, A. B. Rate Constants for the Decay and Reactions of the Lowest Electronically Excited Singlet State of

Molecular Oxygen in Solution. An Expanded and Revised Compilation *J. Phys. Chem. Ref. Data* **1995**, *24*, 663-677.

(33) Dalla Mora, A.; Contini, D.; Pifferi, A.; Cubeddu, R.; Tosi, A.; Zappa, F. Afterpulse-like Noise Limits Dynamic Range in Time-gated Applications of Thin-junction Silicon Single-photon Avalanche Diode *Appl. Phys. Lett.* **2012**, *100*, 4.

(34) Dalla Mora, A.; Tosi, A.; Contini, D.; Di Sieno, L.; Boso, G.; Villa, F.; Pifferi, A. Memory Effect in Silicon Time-gated Single-photon Avalanche Diodes *J. Appl. Phys.* **2015**, *117*, 7.

(35) Losev, A. P.; Byteva, I. M.; Gurinovich, G. P. Singlet Oxygen Luminescence Quantum Yields in Organic-Solvents and Water *Chem. Phys. Lett.* **1988**, *143*, 127-129.

(36) Scholz, M.; Dedic, R.; Breitenbach, T.; Hala, J. Singlet Oxygen-sensitized Delayed Fluorescence of Common Water-soluble Photosensitizers *Photochem. Photobiol. Sci.* **2013**, *12*, 1873-1884.

(37) Gonzalez-Bejar, M.; Montes-Navajas, P.; Garcia, H.; Scaiano, J. C. Methylene Blue Encapsulation in Cucurbit 7 uril: Laser Flash Photolysis and Near-IR Luminescence Studies of the Interaction with Oxygen *Langmuir* **2009**, *25*, 10490-10494.

(38) Stich, D.; Spath, F.; Kraus, H.; Sperlich, A.; Dyakonov, V.; Hertel, T. Triplet-triplet Exciton Dynamics in Single-walled Carbon Nanotubes *Nat. Photonics* **2014**, *8*, 139-144.

(39) Jarvi, M. T.; Niedre, M. J.; Patterson, M. S.; Wilson, B. C. Singlet Oxygen Luminescence Dosimetry (SOLD) for Photodynamic Therapy: Current Status, Challenges and Future Prospects *Photochem. Photobiol.* **2006**, *82*, 1198-1210.